

Influence of Low-Frequency Vibration and Skin Strain on Insertion Mechanics and Drug Diffusion of PVA/PVP Dissolving Microneedles

Vahid Ebrahimejad, Atefeh Malek-khatabi, and Zahra Faraji Rad*

Microneedles (MNs) offer a promising solution for increasing the effectiveness of transdermal drug delivery and diagnostics. However, challenges such as large-scale manufacturing, partial MN penetration, and uncontrolled drug delivery limit the effectiveness of the technology. To overcome these challenges, current research examines the effects of skin strain and vibration on MN insertion and drug delivery. A novel multifunctional impact applicator is developed for improving skin insertion that features a combination of skin stretching, eccentric rotating mass (ERM), and linear resonant actuator (LRA) micro-vibration capabilities. In addition, a scalable replication method for dissolving microneedle patches (DMNPs) are developed using two-photon polymerization (TPP) and soft embossing processes. The DMNPs are used to evaluate the diffusion and concentration of a model drug, fluorescein sodium salt (FSS), when applied using ERM and LRA micro-vibration at different frequencies. Additionally, a new computer simulation method is presented to model the MN insertion into the multilayered hyperelastic skin model, incorporating skin strain and vibrational effects. The results indicate that applying skin strain and vibration decreases the force required for MN insertion and enhances the dissolution and diffusion depth of the drug in the skin, which can enhance the drug permeability and effectiveness of MN devices.

the oral route of administration, TDDs eliminate the first-pass metabolism and harsh environment of the gastrointestinal tract. It can protect the vital body organs, especially the liver, against drug side effects and conserves drug dosage forms from the acidic environment of the stomach.^[1] Despite these advantages, drug administration through the skin is challenging due to the skin stratum corneum (SC) barrier.^[2] Among the third generation of TDDs, MN development is being progressed by clinical trials for the administration of small and macromolecule drugs with great efficiency.^[3,4] TDD via non-invasive MN devices is a promising technique that offers several advantages such as simplicity, reducing sharp and bio-hazardous wastes and the potential for self-administration.^[5] Micro-pores created by MNs in the skin facilitate drug and vaccine delivery.^[6,7] In response to pandemics such as Covid 19, MN patches can enable vaccination through the sustainable release of highly concentrated vaccines to a localized skin

area.^[8-10] MNs also have applications in point-of-care diagnostics, such as sampling ISF for biomarker detection.^[11,12]


MNs are manufactured using various techniques, including laser cutting, laser ablation, lithography, dry/wet etching, reactive ion etching, deep reactive ion etching, micromolding, injection molding, hot and soft embossing, additive manufacturing via 3D printing, and TPP.^[13] Each technique is suitable for fabricating specific materials and has different fabrication times, production costs, accuracy, precision, robustness, and limitations.^[14] Laser cutting and ablation methods are generally used to manufacture solid metallic MNs. These methods are time-effective; however, they are associated with high manufacturing costs, the risk of forming cracks and fatigue due to the thermal effects, and thus are unsuitable for mass production.^[14,15] Lithography requires subsequent dry/wet etching processes to form the final MN shape. Despite the high popularity of the method, it is a multi-step process, which results in an extended manufacturing time.^[16] Additive manufacturing (AM) by conventional 3D printing of MN prototypes is a cost-effective method with high throughput.^[2] Conventional 3D printing offers low accuracy and resolution of the printed parts.^[14] AM via the TPP technique is an alternative method for manufacturing complex 3D

1. Introduction

Transdermal drug delivery systems (TDDs) through skin layers are among the safest routes of drug administration. Compared to

V. Ebrahimejad, Z. Faraji Rad
School of Engineering
University of Southern Queensland
Springfield, Queensland 4300, Australia
E-mail: zahra.farajirad@usq.edu.au

A. Malek-khatabi
Department of Pharmaceutical Biomaterials and Medical Biomaterials
Faculty of Pharmacy
Tehran University of Medical Sciences
Tehran 1417614411, Iran

 The ORCID identification number(s) for the author(s) of this article can be found under <https://doi.org/10.1002/admt.202301272>

© 2024 The Authors. Advanced Materials Technologies published by Wiley-VCH GmbH. This is an open access article under the terms of the [Creative Commons Attribution-NonCommercial](https://creativecommons.org/licenses/by-nc/4.0/) License, which permits use, distribution and reproduction in any medium, provided the original work is properly cited and is not used for commercial purposes.

DOI: 10.1002/admt.202301272

geometries with high precision and sub-micron resolution; however, TPP is still a slow process, thus mainly used for prototyping.^[17] Micromolding is used to replicate MNs from a master and a polydimethylsiloxane (PDMS) negative mold. Micromolding is a cost-effective approach for replicating polymer MNs such as poly(vinyl alcohol) (PVA), poly(vinylpyrrolidone) (PVP),^[18] or thermoplastics.^[17,19] Techniques such as injection molding and hot and soft embossing also promise low-cost methods for MN mass-scale productions.^[14]

MNs are categorized into solid, coated, hollow, hydrogels, and dissolving types designed to serve specific therapeutic purposes. These microdevices are fabricated using various materials, including metal, silicon, polymers, silica glass, and ceramics.^[20] Solid MN patches are generally manufactured with metals, silicon, and recently thermoplastic cyclic olefin polymer (COP) polymers,^[21] which possess high mechanical strength. Uncoated solid MNs create micro pathways to enhance skin permeability before the topical application of a drug.^[22,23] Drug-coated solid MNs can deliver a small amount of the target drug with a rapid decay in drug concentration over time.^[24] The amount of drug dissolution using coated MN patches depends on coating thickness and MN size.^[25] Solid and coated MNs are frequently studied for drug delivery; however, they have limited drug transport through the skin due to their structure and the amount of drug that can be loaded.^[26] Hollow MNs are made from silicon, metal, glass, and polymers, which allow for the transfer of a more significant amount of fluid formulation by diffusion using pressure, capillary or electrically driven forces.^[22,27] The MN bore size and release pressure define the drug transport kinetics through hollow MNs.^[23,28] Hollow MNs are capable of enhanced and precise drug delivery but still require costly and complicated manufacturing setups.^[29]

Hydrogel-forming MNs are used for both drug delivery and biofluid sampling. The MNs will swell upon insertion into the skin due to the hydrophilic nature of the hydrogels.^[17] Hydrogel-forming MNs are used for TDD of drugs by loading drugs into their polymeric structure during manufacturing or into a separate reservoir, which is connected to the MNs for delivery.^[30,31] Dissolving MNs are made from biodegradable polymer matrix or sugar-containing active substances, enabling sustained drug cargo dissolution over time without leaving residues.^[2,32] This delivery method encapsulates drugs inside the polymeric matrix of DMNPs to facilitate sustained delivery of a higher dose of pharmaceuticals.^[33,34] The kinetic and dissolution rates of therapeutic payloads depend on the polymeric composition and fabrication process. Drug release can be through water-soluble polymers such as PVP, PVA, carboxymethyl cellulose (CMC), dextran or via biodegradable compositions including poly(lactide-co-glycolide) (PLGA), poly(lactic acid), chitosan, or poly(glycolic acid).^[22,35]

To achieve efficient TDD, MNs must penetrate through the SC barrier, the outermost layer of skin.^[36] SC consists of elongated dead corneocytes joint by interstitial lipid matrix,^[37] which is the most compact skin layer in dry conditions.^[38] MN partial penetration is mainly associated with skin nonlinear viscoelastic properties, irregular surfaces, and the tendency to fold around MN projections.^[39–42] These conditions may cause early failures, such as MN buckling and bending.^[20] To overcome this challenge, the safety margin (SM) is defined as the ratio of MN failure force to

MN insertion force (F_{ins}) (the maximum force reached before SC rupture).^[21] One of the methods to improve SM is optimizing the geometrical parameters to reduce the F_{ins} .^[43] For example, increasing MN interspacing,^[44] reducing tip diameter,^[43,45] optimizing MN width and tip angle affects the F_{ins} .^[45] In addition, using auxiliary tools such as applicators, applying vibration and increasing insertion velocity with an applicator has been shown to reduce the F_{ins} and facilitate the penetration.^[43,44] Yang and Zahn studied MN insertion on excised animal skin to evaluate the effects of vibration on the MNs insertion using an unspecified frequency. The results demonstrated a > 70% reduction in F_{ins} from ≈ 0.28 to 0.08 N.^[46] However, this study did not indicate the range of applied frequencies nor the effects of the vibration on various stages of MN insertion, such as the insertion and the extraction phase.

Upon improving the SM, penetration efficiency and optimizing the geometrical parameters of the microstructure, the MN drug delivery will be enhanced. For instance, Al Qallaf et al. indicated that specific MN shapes, such as cylindrical/rectangular cuboids, in addition to the number of projections within a patch, can influence the insulin concentration within the blood samples (ng mL^{-1}). This study also showed that MN interspacing, MN thickness, and penetration depth had less significance on insulin delivery.^[47] External factors such as iontophoresis can also improve drug transport through the skin. This technique involves generating an electric potential gradient across the skin.^[23] Niamlang and Sirivat reported that using electric fields from 0 to 0.1 V improved the drug diffusion coefficient ($\text{cm}^2 \text{s}^{-1}$) by 357.8%.^[48] However, iontophoresis alone cannot transport the macromolecules through the SC barrier, indicating the need for combining the technique with MN devices to improve the permeability.^[29] Enhancing permeability can also be achieved via sonophoresis, which involves ultrasonic vibration (>20 kHz). However, this method induces thermal effects on the skin subjects and requires sophisticated instrumentation.^[49] Moreover, vibration and agitation speeds are reported to enhance drug dissolution and delivery.^[50–52] Seeger et al. analyzed and tested the early studies conducted by Beyer and Smith on the dissolution rate of tolbutamide (used for the treatment of non-insulin-dependent diabetes mellitus),^[53] and the Embil and Torosian studies on enteric-coated aspirin,^[54] and confirmed the strong effects of increasing vibration on the drug dissolution time at a low agitation speed of 50 rpm.^[50] Liu et al. studied the impact of vibration at 3200, 4800, and 6400 rpm on drug dissolution. They concluded that an increase of low-frequency vibrations from 3200 to 6400 rpm indicated a \approx five-fold increase in tetramethylpyrazine hydrochloride (TMPH) permeation over time, a drug used for the treatment of cardiovascular and cerebrovascular diseases.^[51] These studies show that drug dissolution strongly depends on drug properties, formulation, dissolution method,^[50] and application technique. Thus, to better understand drug dissolution mechanics, studies need to investigate the drugs with different molecular weights and various methods of excitations, such as low-frequency LRA and ERM.

The current study investigates the effects of external factors, such as variable skin strain and vibration excitations, on MN skin insertion and penetration efficiency. The experiments on the skin model provide insight into the effects of strain and vibrations on MN insertion and extraction mechanics. Moreover, the

dissolution kinetics and concentration levels of the model drug are determined and compared for low-frequency vibrations using both ERM and LRA modes. The study also presents a cost-effective, fast, and mass-scalable method for manufacturing highly accurate DMNPs replicated using a PVA/PVP polymeric formulation. The proposed replication process involves using TPP to print primary masters and a soft embossing technique to create the secondary masters. The new approach overcomes the challenge associated with the slow TPP process and enables simultaneous replication of highly accurate DMNP replicas in a rapid and cleanroom-free process. Despite the lack of finite element analysis (FEA) investigations on the impact of external simulators, such as vibration and skin strains, on MN insertion, the current study introduces an FEA method to evaluate the MN insertion mechanics into the multilayered hyperelastic skin model under the external effects of vibrations and skin strain.

2. Experimental Section

2.1. Master MN Array Design and Fabrication

Consistent with the previous studies, 3D laser lithography using the Nanoscribe Photonic Professional GT 3D printer (Nanoscribe GmbH, Karlsruhe, Germany) was employed to fabricate the master mold.^[19,24,55] In summary, the 3D designs of a 9×9 master MN array and a single master MN (single MNs were fabricated to be used for mechanical compression and bending tests only) were created using SolidWorks (Dassault Systems SolidWorks Corporation, Concord, NH, USA) with an overall height of 1100 μm, 75 μm base fillets, and 500 μm interspacing for the MN array. The stereolithography (STL) codes from SolidWorks were imported into the DeScribe (Nanoscribe GmbH, Karlsruhe, Germany) software to specify print settings tailored to the design. The models were printed separately with 100 mW laser power, scanning speed of 100 mm s⁻¹, and shell and triangular scaffolds with 20 μm wall spacing. Parameters such as 2 μm slicing distance, four base slice counts, null shear angle (0°), and 0.6 interface position were used to reduce print time and sample delamination from the substrate. The output GWL file, which stored the printing specifications, was further imported into NanoWrite software (NanoScribe GmbH, Karlsruhe, Germany) linked to the NanoScribe system for printing.

The TPP system incorporates a pulsed erbium-doped femtosecond fiber laser source with a center wavelength of 780 nm for exposing the photoresist. Based on the two-photon absorption theory, when the combined energy of two photons surpasses the absorption energy threshold of the photoresist, the nonlinear response occurs at the focused point, which enables the polymerization of high-resolution structures.^[56] Initially, a drop of negative-tone IP-S photoresist (Nanoscribe GmbH, Karlsruhe, Germany) was cast onto the indium tin oxide (ITO) conductive side of a glass substrate and inserted into the NanoScribe system. The objective lens with × 25 magnification and NA of 0.8 focused the laser beam into the photoresist. MN structures were then written in galvo scan mode in the X and Y directions and piezo offsetting mode in the Z direction. Following the print, the samples were further developed for 10 min in propylene glycol monomethyl ether acetate (PGMEA) solution, then rinsed for 2 min in isopropyl alcohol (IPA), and finally air-dried.

2.2. Casting Negative PDMS Mold for Replication of Thermoplastic MN Arrays

PDMS (SYLGARD 184 Silicone Elastomer Kit, Dow Corning, Midland, MI, USA) was used for creating a negative mold of the master MN array. A 1:10 curing agent/base solution was initially mixed and then degassed in a planetary mixer for air bubble removal. PDMS solution was then poured on the MN array printed via TPP in a petri dish and cured for 2 h inside the oven at 80 °C. Finally, the soft negative PDMS mold was peeled off from the MN master for replication. A similar process was conducted to create a negative PDMS mold of the single MN.

2.3. Fabrication of Secondary Master MN Arrays Using Thermoplastics

The PDMS negative mold of the master MN array was placed between 40 mm diameter rheometer plates (TA Instruments, New Castle, USA). A total of four pellets (cyclo-olefin polymer, Zeonor 1060R) were placed on the PDMS cavities, and the chamber temperature was increased to 163 °C, which is 63 °C above the thermoplastic glass transition temperature ($T_g = 100$ °C). While keeping the lower plate fixed, the upper plate was lowered as a function of time to press the melted thermoplastic pellets into the PDMS cavities while limiting the axial force to 21 ± 3 N. To control the axial force and prevent damage to the PDMS molds, upper plate downward displacement was reduced over time based on a nonlinear model from 100 μm per interval to 25 μm for 1 h until the upper plate reached 200 μm above the PDMS surface.^[55] The chamber temperature was then reduced to 10 °C for 15 min for thermoplastic solidification. Upon solidification, replicas were peeled off the soft PDMS mold (Figure 1a). The process was repeated eight times to create eight thermoplastic MN arrays to be used as the secondary master MN arrays.

2.4. Replication of PVA/PVP DMNPs

The eight thermoplastic MN masters were used as secondary masters for fabricating eight negative PDMS molds for PVA/PVP DMNPs replication. Thus, the thermoplastic MNs underwent a similar process described in Section 2.2 to make the PDMS negative molds. A PDMS ring was attached to each mold using PDMS to PDMS bonding by oxygen plasma (Pie Scientific, California, USA). The PDMS molds were then cured at 80 °C for 15 min before cutting them to fit into the 50 mL centrifuge tube (Figure 1b). The rings surrounding the PDMS cavities acted as liquid solution containers for centrifugation.

The PVA, PVP, and FSS were purchased from Sigma–Aldrich (Sigma–Aldrich Corp., St. Louis, MO, USA) to prepare the model drug solution. PVA 30 kDa (15% w/v) was slowly added to 20 mL of DI water, stirred at 750 rpm for 1 h at 60 °C, and placed inside an ultrasonic bath for 2 h for further dissolution. PVP 40 kDa (50% w/v) was then gently added to the solution and stirred until dissolved. A separate solution of FSS (0.4% w/v) in 2 mL ethanol 70% was then added to the PVA/PVP solution and stirred for 30 min at 60 °C until dissolved.

To create DMNPs, 50 μL of PVA/PVP/FSS solution was placed on each PDMS mold. The molds were then carefully placed

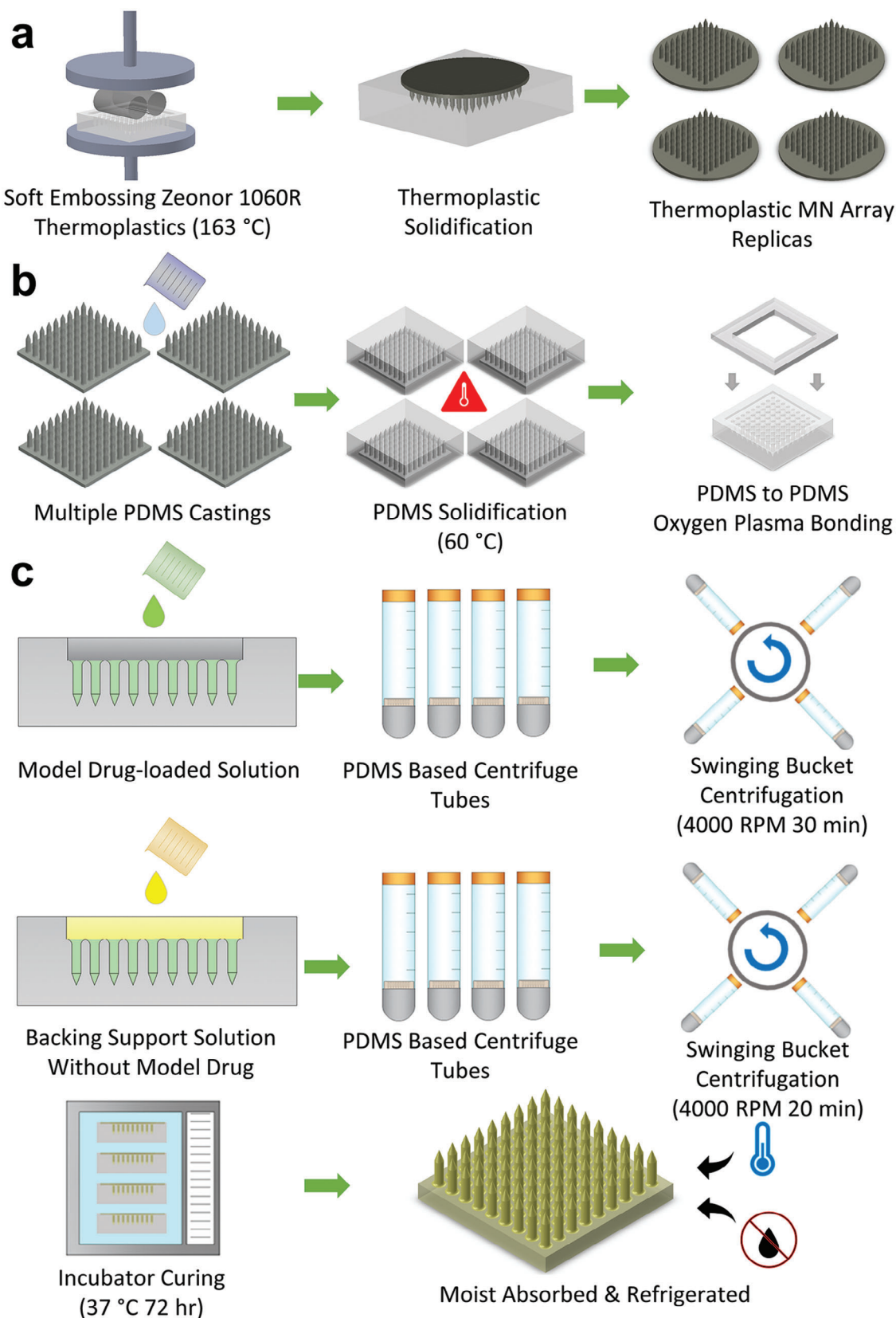


Figure 1. Replication process of PVA/PVP DMNPs a) multiple replications of thermoplastic MN patches using the soft embossing technique, b) creating multiple PDMS negative molds from the replicated thermoplastic MNs, c) replication of PVA/PVP DMNPs via PDMS negative molds and centrifugation.

inside 50 mL centrifuge tubes. During each replication process, eight sample tubes were centrifuged simultaneously using Allegra X-30 swinging bucket centrifuge (Beckman Coulter, Brea, USA) at 4000 rpm for 30 min. The molds containing the solutions were kept inside a laboratory oven for 2 h to initiate solidification. In the next step, 100 μ L of PVA/PVP solution without the model drug was poured on each partially dried mold and centrifuged at 4000 rpm for 20 min. The excess solutions were removed, and the PDMS molds were kept inside an incubator at 37 $^{\circ}$ C for another 72 h. Once MN patches were peeled off from the molds, they were refrigerated until further use (Figure 1c). Similar procedures were performed to replicate the single PVA/PVP MNs for compression and bending tests.

2.5. Mechanical Strength Testing of MNs

The mechanical strength of PVA/PVP DMNPs was investigated on single PVA/PVP MNs using axial compression and lateral bending tests. Both tests were conducted using the TRIOS package linked with the TA hybrid rheometer previously used for soft embossing (Section 2.3). During the axial compression test, the PVA/PVP MN was attached to the lower disk with double-sided tape while the upper disk of the rheometer was lowered to measure the force of fracture. The bending test was performed by attaching the PVA/PVP MN to a 90 $^{\circ}$ custom-made metal stub using double-sided tape. A premade metallic block was attached to the upper disk of the rheometer and lowered during the test. The metal block provided uniform contact with the PVA/PVP MN tip to apply the lateral force. During the two tests, force and displacement data were recorded to determine the mechanical behavior and failure points. Data were then plotted by MATLAB (Natick, MA, USA) software to be compared against the theoretical models.

2.6. Scanning Electron Microscopy

The morphology and dimensions of PVA/PVP DMNPs and mechanically tested MNs were measured using a scanning electron microscope (SEM, JOEL JSM-7001F). Samples were coated with a 10 nm layer of platinum using JOEL Desktop Sputterer. To measure the length and base diameter of DMNPs, a 90 $^{\circ}$ angled metal stub was used to hold the samples. The secondary electron detector with an accelerating voltage of 2 kV in high vacuum mode was used for mechanically tested MNs. However, the accelerating voltage was increased to 10 kV to enhance the field depth for imaging the PVA/PVP DMNPs.

2.7. Manufacturing Featured Impact Applicator

The novel spring-loaded applicator was designed in SolidWorks software (Dassault Systems SolidWorks Corporation, Concord, NH, USA). The model was then printed using a Teirtime X5 3D printer (Teirtime Corporation, Milpitas, CA, USA) from polylactic acid (PLA) filament. This applicator was the advanced version of the impact applicator used in previous studies.^[24,55] The new design can adjust impact velocity, enabling two regulatable

ERM/LRA vibration modes and is equipped with a skin stretching mechanism. The typical peak-to-peak vibration amplitude of ERM and LRA devices at the voltage of 3 V were 1.2 and 1.13 G, respectively.

The impact velocity control mechanism had a grooved plunger and a top screw for velocity regulations, enabling velocities of 1.5, 3, and 4.5 m s^{-1} and impact energies of 23.94, 95.76, and 215.46 mJ. The impact plunger had a combined weight of 21.28 gr, which includes PLA plunger and ERM/LRA micro-vibration devices. The plunger was fixed by the locking mechanism and released by pressing the push button (Figure 2a). While the grooved plunger enables exact impact velocities of 1.5, 3, and 4.5 m s^{-1} , minute adjustments using the top screw can give a broader range of impact velocities ranging from 1.5 to 5.5 m s^{-1} . A high-speed camera and theoretical models were used to measure the impact velocity of the current prototype, as described in the previous study.^[24]

The applicator's skin stretching mechanism was incorporated with stretching arms equipped with torsion springs for direct skin extension and compression springs for the applicator settlement on the skin surface through height adjustments (Figure 2b). To apply two modes of vibration, LRA and ERM micro-vibration devices with $\approx 50 - 250$ Hz frequency range were purchased from Precision Microdrives (London, UK) and inserted into the slots in the plunger plate where the DMNPs attach. A custom-made electronic circuit was built to switch and regulate the microdriver frequencies. The circuit contained a 5 k Ω potentiometer, a 510 Ω resistor, and a NPN 2N2222a transistor with an ON/OFF switch to regulate the LRA/ERM vibrations. This circuit was powered by a 3.7 V polymer lithium-ion battery (Ecocell, Castle Hill, New South Wales, Australia) equipped with a MicroUSB Lilon/LiPoly charger jack (Adafruit Industries, New York City, New York, USA). The LRA and ERM frequency ranges were measured and recorded using digital multimeters in a series of current and voltage tests against the manufacturer performance graphs (Figure 2c).

2.8. Evaluation of Strain and Vibration on Mechanics of MN Insertion and Extraction

MN insertion and extraction mechanics were studied to determine the effects of strain and vibration on the SM. As a skin model, a PDMS sample with 4 ± 0.1 mm thickness was placed on the 3D printed PLA platform and then fixed by the skin stretching mechanism. The strain ($\epsilon = \Delta l / L_0$) to stretch (Δl) ratio of the mechanism is 0.0086 mm^{-1} , where Δl is the value of stretch (mm), and L_0 is the length of porcine skin (mm) fixed by each end of the mechanism (Figure 3a). To prevent the early contact of the PVA/PVP DMNP base with the skin model, an alternative 4 mm BD Ultra-Fine PEN Needles (Franklin Lakes, New Jersey, USA) for insulin injection was used. In the previous study by Park et al., the interface area of polymeric MNs inserted into the human cadaver skin showed the most influence on the insertion mechanics compared to other geometrical features.^[57] Thus, PEN needles with a similar base diameter (230 μm) and tip size (1.6 μm) were assumed to be the suitable replacement for this particular study for the PVA/PVP DMNPs.^[55] The PEN needles were attached to the rheometer upper plate using double-sided

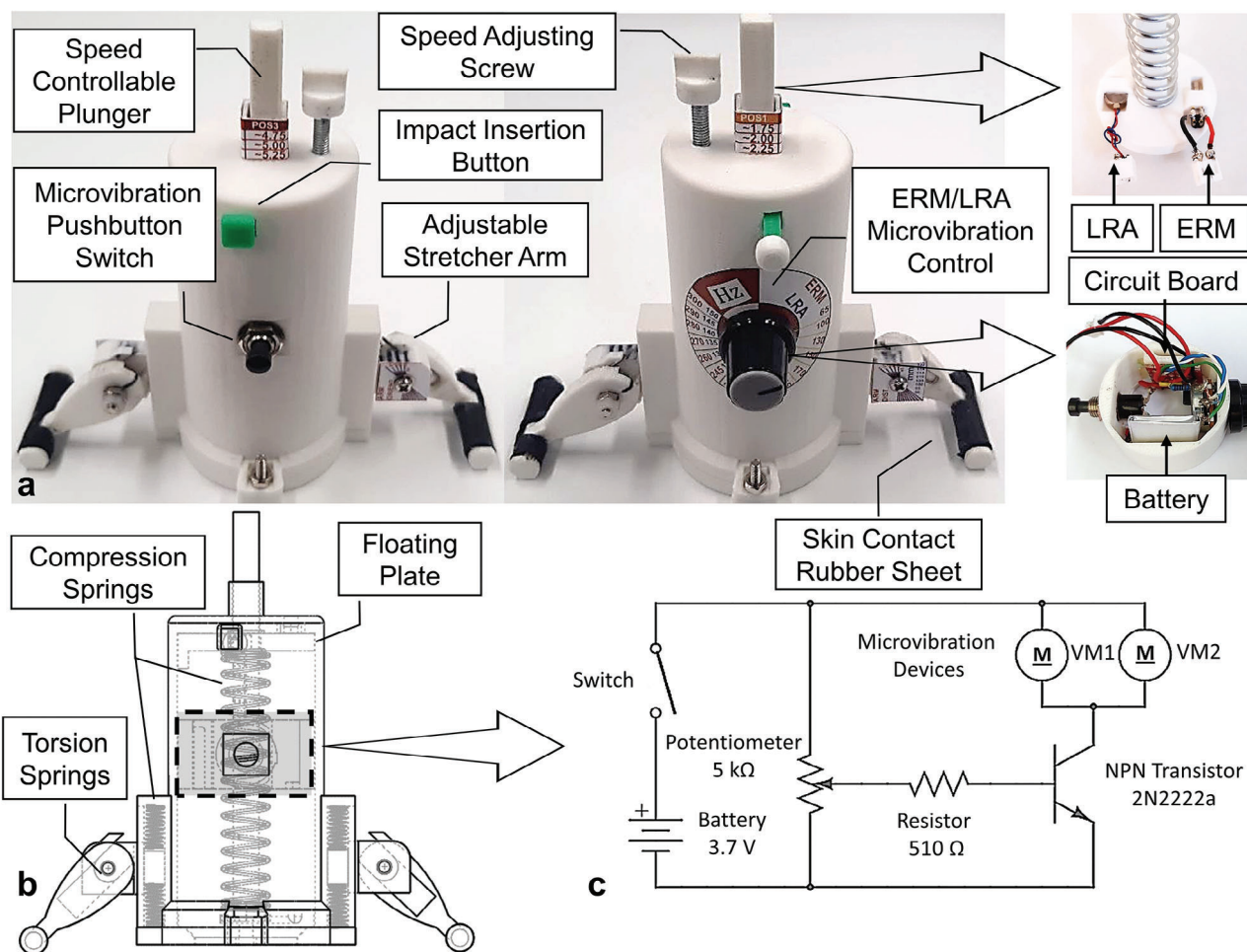


Figure 2. The impact applicator for insertion of MNs into the skin. The 3D printed prototype features regulatable impact velocity, stretching arm mechanism, and ERM/LRA vibration systems. a) The spring-loaded impact velocity can be regulated via preset velocities ($1.5, 3, 4.5 \text{ m s}^{-1}$) on the grooved plunger or minute adjustments to the floating plate using the top screw. The skin insertion is triggered using the locking mechanism by pressing the push button. Skin stretching can be performed using the extendable side arms. Two pairs of compression springs enable the applicator settlement on the skin surface through height adjustment before the torsion springs can initiate skin extension directly. b) A cross-sectional view of the applicator showing compression and torsion springs and floating plate. c) To regulate the ERM/LRA vibrations, an electronic circuit containing a 3.7 V polymer lithium-ion battery, 5 k Ω potentiometer, 510 Ω resistor, 2N2222a NPN transistor, and MicroUSB charger port with ON/OFF switch was built to control the vibration frequency.

tapes. While force-displacement data were recorded, the needle was inserted and extracted by 4 mm into the skin model. As shown in Figure 3a, insertion tests were conducted with various strains of 0 to 0.2 and vibration ranges of 0, 50, 150, and 250 Hz. These strains on the porcine skin were made by adjusting the two screws on the stretching mechanism at 0%, 5%, 10%, and 20% from the skin's unstretched condition.

2.9. Skin Insertion and Diffusion Study of DMNPs

The penetration efficiency, drug diffusion, and concentration of the model drug encapsulated in DMNPs were studied using porcine abdominal skin. These studies were performed with experimental procedures approval obtained from the University of Southern Queensland (UniSQ) and the University of Queensland (UQ) animal ethics (Ethics Number: 20EXE005) and

biosafety committees (Biosafety Number: 21BIOS003). Porcine cadaver skin was shaved and sliced into $3 \pm 0.1 \text{ mm}$ sizes using scalpel blades, and the fat layer was removed from underneath the skin. The skin tissue was kept at $-20 \text{ }^\circ\text{C}$ and naturally thawed before insertion tests. A previously reported stretching mechanism capable of accurately adjusting skin strain was used during the tests.^[24,55] The porcine skins were stretched by $\approx 5\%$ from the undeformed state to mimic the skin in vivo condition. A total of 32 DMNPs were tested on the porcine skin. For each test, a DMNP was attached to the applicator's plunger using double-sided tape and then inserted into the skin at 3 m s^{-1} using 0, 50, 100, 150, and 200 Hz ($n = 4$) for LRA and 0, 50, 150, and 250 Hz ($n = 4$) for ERM-induced vibrations for 4 min (Figure 3b). Penetration and diffusion of the FSS drug model were then examined after 20 min with a confocal microscope (CLSM, Zeiss LSM710, Germany) using Z-stack and tile scan techniques with run times of $\approx 20 \text{ min}$.

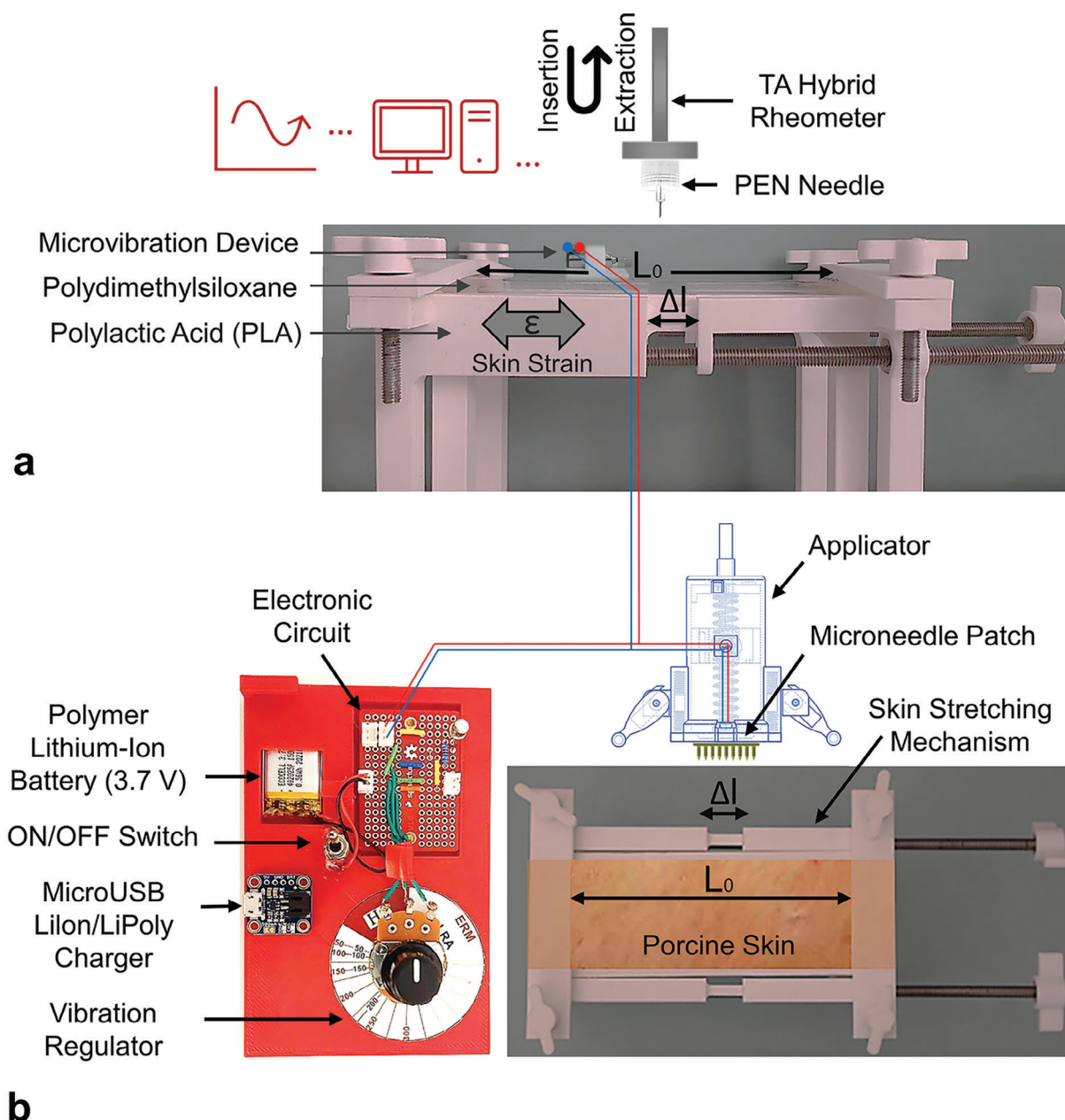


Figure 3. The experimental setup for a) insertion tests on porcine skin using the applicator incorporating vibration to quantify model drug diffusion and b) PEN needle insertion tests using a rheometer, including the effects of skin strain and vibration on insertion and extraction mechanisms.

2.10. Liquid Chromatography Mass Spectrometry (LC-MS) Analysis

To determine the concentration of the model drug, LC-MS analysis was conducted using a Thermo U3000 HPLC coupled to a Bruker Micro TOF Q II (Bruker Corporation, Massachusetts, USA). LC-MS analysis was performed using a C18 HPLC column (Phenomenex Kinetex 100 A, $50 \times 2.1 \text{ mm} \times 2.6 \mu\text{m}$) at $200 \mu\text{L min}^{-1}$. Buffer A was 18.2 M ohm purified water with 0.2% formic acid, and buffer B was 80% Acetonitrile (aq) with 0.2% formic acid. A gradient was established at 40°C starting at 10% buffer B for 2 min, followed by a linear ramping to 65% B over 7 min.

This was followed by a linear ramping to 100% B over 12 s and held at 100% for 1 min. It was then returned to 10% B over 12 s and held at 10% for 2.6 min. The first 2 min of each analysis were diverted to waste. The microTOF Q II was operated in positive mode with nebulizer gas at 0.4 bar, dry gas at 4 L min^{-1} , dry temperature at 200°C , transfer time of $70 \mu\text{s}$, pre-pulse storage of $5 \mu\text{s m z}^{-1}$ 50–1000, and spectra time of 2 s. During the test, the collisional sweeping varied from 150 to 600 Vpp. The acquisition was controlled using Hystar3.2 SR2, MicroTOF Control 1.3, and Chromeleon 6.8. The data was visualized using Data Analysis 4.0 and Quant Analysis 2.0. The MicroTOF Q was calibrated before testing each sample batch using ESI-L tuning

mix – p/n 1969–85000. During the LC-MS analysis, the FSS calibration curve was created using different FSS/Milli-Q water solutions standards (1:1000, 2:1000, 1:10 000, 2:10 000 v/v), which yielded an accuracy of $R^2 = 0.99$.

2.11. FEA of MN Insertion into Skin with Strain and Vibration Effects

A specific simulation paradigm using ANSYS (2020 R1, ANSYS, Canonsburg, Pennsylvania, USA) was created to evaluate the mechanics of MN insertion into the skin when applying strain and vibration. For skin strain models, the stretching of the skin was modeled in the Static Structural module, which is linked to the Explicit Dynamics module used for modeling the MN insertions. The vibration simulation was initiated by introducing the results from the Modal and Harmonic Response modules into the Static Structural module, which is further linked to the Explicit Dynamics for the MN insertion model. Based on Equation 1, a sinusoidal forced vibration was assumed for the insertion of MN into the skin model incorporating vibration,

$$M\ddot{x} + c\dot{x} + kx = me\omega^2 \sin(\omega t) \quad (1)$$

where m is the weight of the rotating mass, e is the eccentricity, and ω is the vibration frequency. The XYZ displacements from the vibration excitation were imported to the Static Structural module using the External Data module. The MN insertion model is then performed using the Explicit Dynamics module. The skin model was assumed to comprise three layers: 1) SC, 2) dermis, and 3) hypodermis, with thicknesses of 26 μm , 2 mm, and 1.1 mm, respectively. Ogden model (first order) material properties were specified for the dermis layer.^[58] However, the SC and hypodermis layers were assumed to possess linear elastic responses. Quadrilateral meshing with a bias factor of 10 was used to generate smaller elements in the vicinity of MN-skin interfaces. The friction coefficient of 0.42 was applied between the contact surfaces.^[59] MNs were inserted into the skin layers with a velocity of 3 m s^{-1} while recording the force-displacement data. The erosion algorithm setup enabled the piercing of MNs into the skin by eliminating elements reaching the failure stress while maintaining their inertia effect. Moreover, automatic mass scaling with a minimum Courant–Friedrichs–Lewy (CFL) time step of 1 picosecond was used to reduce the simulation run time.^[60] The mass scale algorithm was used to artificially increase the elemental density by increasing the time required for a sound wave to traverse the smallest elements. **Table 1** shows the material properties that were allocated to MN and individual skin layers.

2.12. Statistical Analysis

Morphological measurements, mechanical failure points, diffusion, and model drug concentrations were presented as the mean \pm standard deviation ($n = 4$). Standard deviations from the mean were expressed by error bars. Statistical analysis was also performed using one-way ANOVA to compare model drug diffusion and concentrations. For this study, the p -value was set at $p < 0.05$

Table 1. Material properties applied for MN and multilayered human skin model in ANSYS explicit dynamics.

Parameter	MN	SC	Dermis	Hypodermis
Mathematical model	Linear elastic	Linear elastic	Hyperelastic: Ogden 1 st order	Linear elastic
Thickness (mm)	–	0.026	2	1.1
Young Modulus (MPa)	1400	139	–	0.1
Poisson ratio	0.48	0.49	0.49	0.48
Density (kg mm^{-3})	1.3 E-6	1.3 E-6	1.2 E-6	9.71 E-7
Hyperelastic Coefficients MU1, A1 (MPa)	–	–	0.0977, 16.09	–
Incompressibility factor (MPa^{-1})	–	–	0.0745	–
Failure criteria (MPa)	–	20	7	–
Refs.	[61]	[59,62]	[59,63]	[59]

for the statistical significance. Microsoft Excel (Office 365, Microsoft Corporation, Redmond, WA, USA) was used for statistical calculations.

3. Results

3.1. Fabrication of DMNPs

The 9×9 master MN array was printed from IP-S photoresist using the TPP technique in ≈ 20 h with submicron resolution. The master MN array was used to create a PDMS negative mold to replicate thermoplastic MNs. Thermoplastic (Zeonor 1060R) MN arrays were replicated using a hybrid rheometer in ≈ 1 h using the PDMS negative mold and soft embossing process. Due to the long printing time of the TPP process, the manufacturing process is only suitable for prototyping; therefore, the replicated thermoplastic MNs were used to produce multiple secondary negative molds of the master. Eight negative PDMS molds were created from the thermoplastic MN masters in a relatively short process. Subsequently, a total of 35 PVA/PVP DMNPs were made using micromolding with swinging centrifugation and heat treatment in a standard laboratory incubator. SEM measurements of the replicated DMNPs showed an average of $951.95 \pm 3.38 \mu\text{m}$ ($n = 3$) overall height, $218.81 \pm 5.18 \mu\text{m}$ ($n = 3$) base diameter, and $6.45 \pm 0.42 \mu\text{m}$ ($n = 3$) tip diameter. These data indicated $8.91 \pm 0.32\%$ longitudinal and $14.32 \pm 2.03\%$ lateral shrinkages compared to the thermoplastic secondary masters. This also shows a longitudinal shrinkage of $13.46 \pm 0.31\%$ and lateral shrinkages of $12.48 \pm 2.07\%$ from the original geometrical parameters (250 μm base diameter, 1100 μm height). During the soft embossing and micromolding processes, no defects were observed on the PDMS molds. **Figure 4** shows the SEM images of the arrays made from the TPP process using IP-S photoresist, Zeonor 1060R thermoplastic MNs, and PVA/PVP DMNPs.

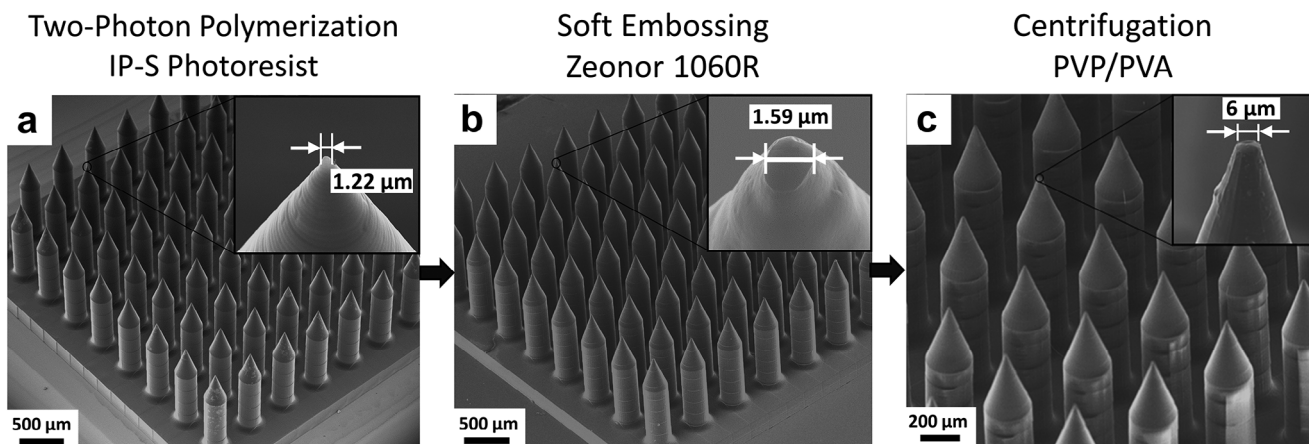


Figure 4. SEM images of a) 9x9 MN array fabricated using TPP as the primary master, b) secondary master replicated via soft embossing of thermo-plastics (Zeonor 1060R), c) PVA/PVP DMNPs replicated from the secondary masters using PDMS molds and micromolding technique with $\approx 6 \mu\text{m}$ tip diameter.

3.2. MN Mechanical Strength

To evaluate the mechanical behavior and failure points, quasi-static compression and bending tests were conducted using rheometer parallel plates on single PVA/PVP MNs. The force-displacement graphs of the data indicated a rise which peaked at the failure point before a sharp drop in the data. The compression test results show that the buckling failure force is $0.65 \pm 0.04 \text{ N}$ (Figure 5a), and the bending failure is $0.33 \pm 0.02 \text{ N}$ (Figure 5b).

Based on theoretical models, critical buckling load can also be estimated using the following formula:

$$F_{\text{buckling}} = \frac{\pi^3 a^4 E}{16L^2} \quad (2)$$

where a is the MN radius (0.125 mm), L is the MN effective length (1 mm), and E is the elastic modulus (1400 MPa).^[61] For the

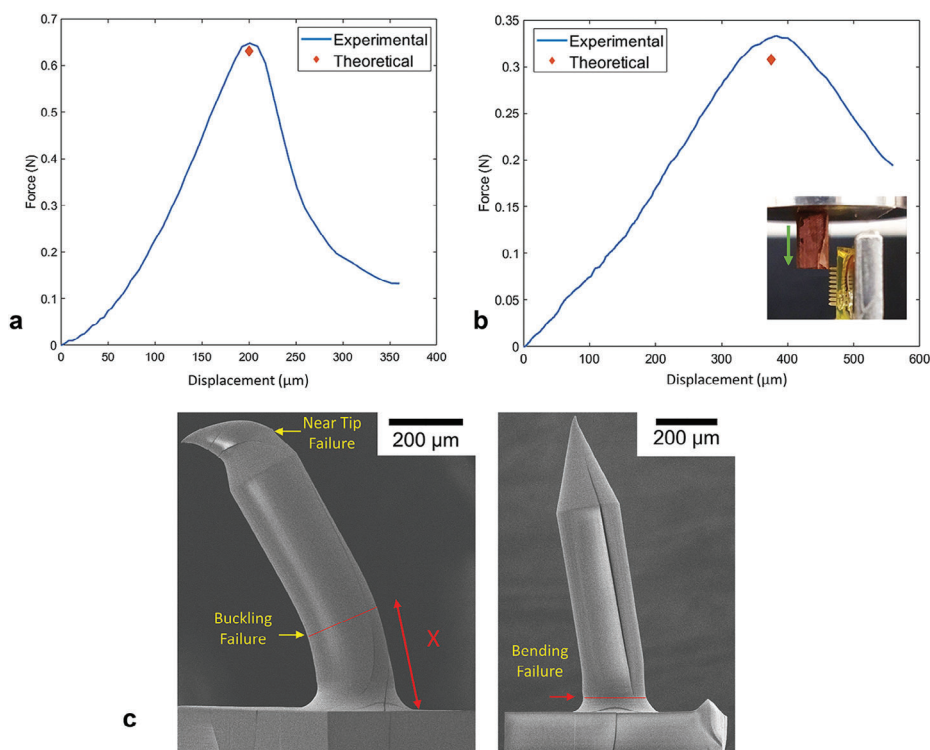


Figure 5. The mechanical testing results, including a) axial compression and b) bending tests on an MN, were compared against theoretical models. c) SEM images of a single MN after compression test indicate near tip and buckling failures at a distance (x) from the base, followed by SEM image of bending failure which occurred at the MN base.

case of bending, the maximum bending load can also be found using:^[64]

$$F_{\text{bending}} = \frac{K_t \sigma_y \pi a^3}{4L} \quad (3)$$

where K_t is the stress correction factor for shafts with base fillets (1.75), σ_y is yield stress (77.4 MPa), a is the MN radius (0.125 mm), and L is the MN effective length (0.675 mm).^[65] Based on theoretical analysis, Equations (2) and (3) predicted that the buckling and bending failures occur at 0.63 N and 0.31 N, respectively, which are in accordance with the experimental results. SEM images of the DMNPs following the mechanical tests are shown in Figure 5c. The compression test indicated a near-tip failure due to direct contact with the metal plate and buckling failure at a distance (x) from the MN base. However, bending failure occurred directly at the MN base, coinciding with the base fillet.

3.3. Effects of Vibration and Strain on Insertion Force of MNs

3.3.1. Experimental Results Using PEN Needle

The effects of vibration excitation and strain were evaluated using a rheometer to measure the insertion and extraction mechanics of PEN needles. The force-displacement data were recorded during the PEN needle insertions and extractions phases. As a skin model, a PDMS sample was subjected to strain using a custom-made stretching tool at 0%, 5%, 10%, 15%, and 20% relative to its unstretched condition.^[55] In each case, the PEN needle was inserted into the sample until it reached a depth of 4 mm and then withdrawn back to the original position. Throughout the experiments, force increased gradually and peaked at F_{ins} before a sudden drop. The extraction phase lay in the negative region with a peak at F_{ext} , steadily returning to the starting point. During the PEN needle insertion phase, an evident reduction in F_{ins} was observed from 0.311, 0.279, 0.24, 0.214, to 0.204 N for strain rates of 0%, 5%, 10%, 15%, and 20%, respectively. A similar trend occurred during the extraction phase, indicating a reduction in the magnitude of extraction force. The results showed that F_{ext} reduced from 0.192, 0.164, 0.109, 0.095, to 0.081 N for strains of 0%, 5%, 10%, 15%, and 20%, respectively (Figure 6a). A similar insertion procedure was applied to test vibration excitations. At 0, 50, 150, and 250 Hz vibrations, F_{ins} were recorded as 0.286, 0.262, 0.258, and 0.251 N, respectively. Similarly, the extraction phase showed reductions in the F_{ext} from 0.093, 0.088, and 0.082 to 0.057 N for vibrations applied at 0, 50, 150, and 250 Hz, respectively (Figure 6b).

3.3.2. FEA Results

FEA analysis of the MN insertion mechanism was conducted using the interconnection of different modules in ANSYS software. Modal, Harmonic Response, External Data, Static Structural, and Explicit Dynamics modules were used to model skin insertion incorporating strain and vibration excitation. The multilayered skin was modeled by planar symmetry, and boundary

conditions were activated at the level of Explicit Dynamics to maintain the results from the Static Structural module (Figure S1, Supporting Information). During the analysis, the insertion force was plotted against the MN displacement penetrating the skin model. The results indicated a rise in the recorded force that peaked at the F_{ins} before a sudden drop at the skin puncture point. Figure 7a shows the effects of increasing vibration excitations from 0 to 50, 150, and 250 Hz on the F_{ins} , showing the F_{ins} have reduced to 0.098, 0.097, 0.096, and 0.078 N, respectively. The drop in F_{ins} became profound upon a further increase in the applied frequency from 150 Hz to 250 Hz. Applying skin strains at 0%, 2.5%, 5%, 7.5%, and 10% also resulted in a reduction of F_{ins} , which were 0.13, 0.123, 0.114, 0.101, and 0.088 N, respectively. Figure 7b shows these force-displacement diagrams for MN-skin insertions with different skin strain rates ranging from 0–10%.

3.4. Effects of Low-Frequency Vibration on Penetration and Diffusion of Model Drug

3.4.1. Diffusion of FSS Model Drug

Confocal imaging was performed to evaluate the penetration depth and diffusion pattern of the DMNPs inside the cadaver porcine skin tissues. Thirty-two tests were conducted to assess the effects of LRA and ERM vibrations on DMNPs when applied to the tissues at 3 m s⁻¹ for 4 min. Figure 8a shows the depth-coded and confocal image of FSS diffusion after ≈30 min post-experiment, which is captured using the Z-stacking technique. The confocal image was used to examine the model drug diffusion of DMNPs influenced by LRA and ERM vibrations at various frequencies ($n = 4$) ranging from 0 to 250 Hz. During the non-vibrated (0 Hz) insertion test, the mean diffusion after ≈30 min ($n = 4$) was to a depth of 246.85 ± 40.96 μm under the skin surface. However, when the ERM vibration excitation of 50, 150, and 250 Hz was introduced, the maximum diffusion of the FSS drug model improved to 273.05 ± 34.98, 324.51 ± 42.40, and 387.68 ± 49.63 μm under the skin surface, respectively. A similar set of experiments were performed using LRA vibrations at 50, 100, 150, and 200 Hz, which resulted in the diffusion of the model drug to a depth of 379.01 ± 25.44, 428.87 ± 14.25, 491.14 ± 21.45, and 532.63 ± 23.69 μm, respectively. All the data were recorded 30 min after insertion. The results showed that increasing the vibration enhanced the PVA/PVP dissolution over a constant holding time of 4 min. Figure 8a shows the optical images of a DMNP after applications on the porcine skin at different vibration frequencies. In all tests, the DMNPs were dissolved during the skin insertion tests, and the drug was delivered into the underlying skin layers.

Another method of evaluating the diffusion of DMNPs was to plot the average FSS intensity for the entire patch versus the overall length. Therefore, Figure 8b represents the improvements in FSS intensity through nine consecutive peaks when the frequency was increased from 0 to 250 Hz. In the case of MNs positioned at the center of the DMNPs, the average FSS intensity was lower than MNs located around the edge of the patch. This indicates the “bed of nails” effects where central MNs have only partially penetrated the skin. Based on the “bed of nails”

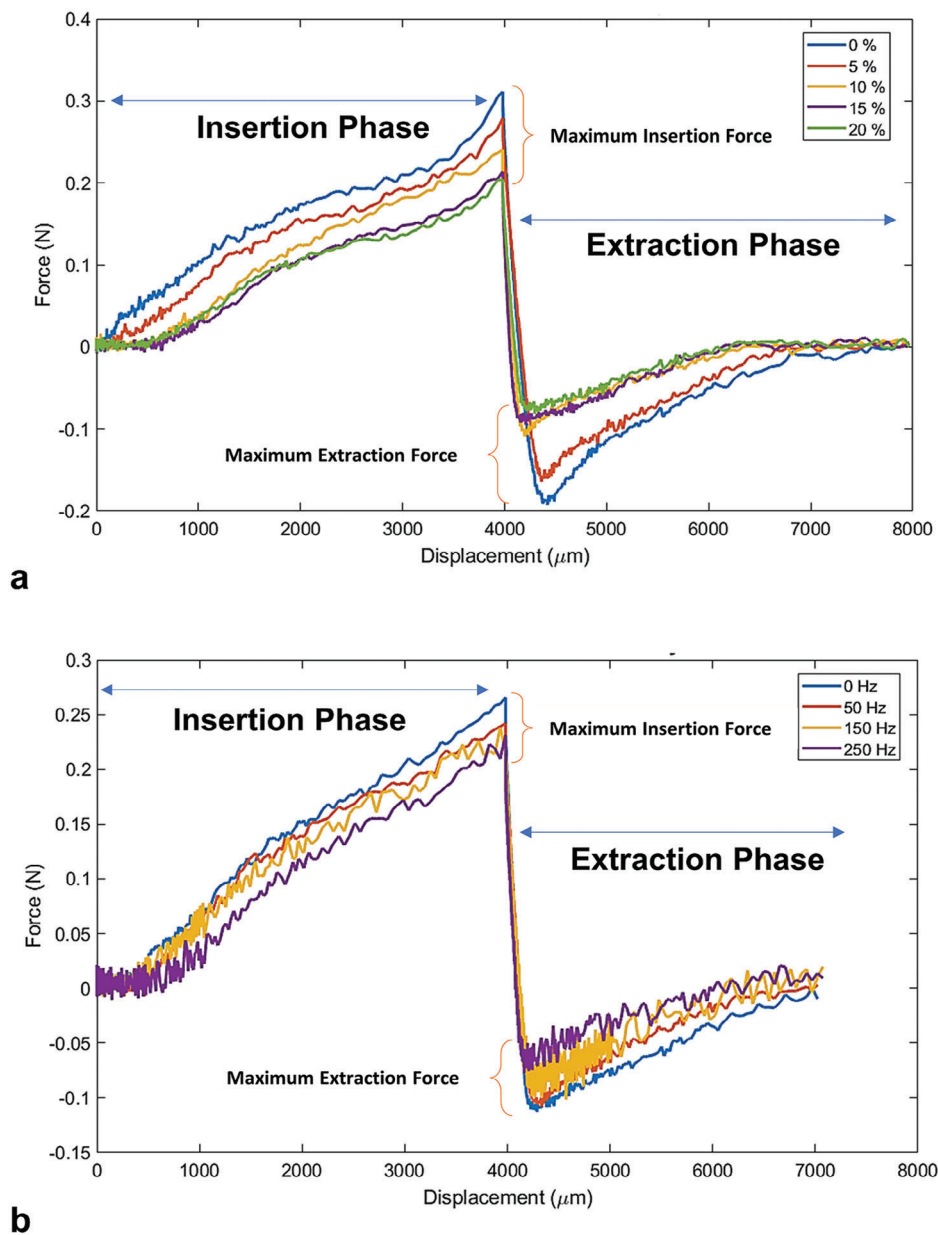


Figure 6. Force–displacement diagrams during PEN needle insertion and extraction phases for varying a) strain rates of 0–20% and b) vibrations excitation ranges of 0–250 Hz.

definition, as the outer MNs have stretched the skin first, the inner MNs require higher pressure to reach a similar penetration depth.^[66] The outcomes from the diffusion analysis using the confocal images were then compared to the FEA simulation of 3 m s^{-1} MN impact insertion at 0, 50, 150, and 250 Hz skin vibration. The data from the impact simulation showed a linear increase in the penetration depth from 161.12, 164.34, and 176.52 to 200.76 μm . Comparing the experimental and simulation results validated the effects of increasing vibration on the overall penetration depth. The higher penetration observed in experimental data is due to the additional diffusion of FSS into the deeper skin layers during the ≈ 30 min post-insertion confocal imaging (Figure 8c).

3.4.2. Concentrations of FSS Model Drug

LC-MS analysis was used to determine the FSS concentration for different vibrational frequencies after each insertion test using the dissolution of DMNPs/Milli-Q water solutions. Calibration curves were developed for FSS solutions based on predetermined concentrations. The ERM-based frequency that ranged between 0, 50, 150, and 250 Hz resulted in concentrations of 2.64 ± 0.14 , 2.78 ± 0.1 , 2.94 ± 0.21 , and $2.93 \pm 0.05 \mu\text{g L}^{-1}$, respectively. Similarly, vibration based on the LRA excitations of 50, 100, 150, and 200 Hz resulted in concentrations of 2.8 ± 0.05 , 2.89 ± 0.07 , 2.96 ± 0.02 , $2.98 \pm 0.03 \mu\text{g L}^{-1}$, respectively. The results showed that inducing 250 Hz ERM frequency and 200 Hz

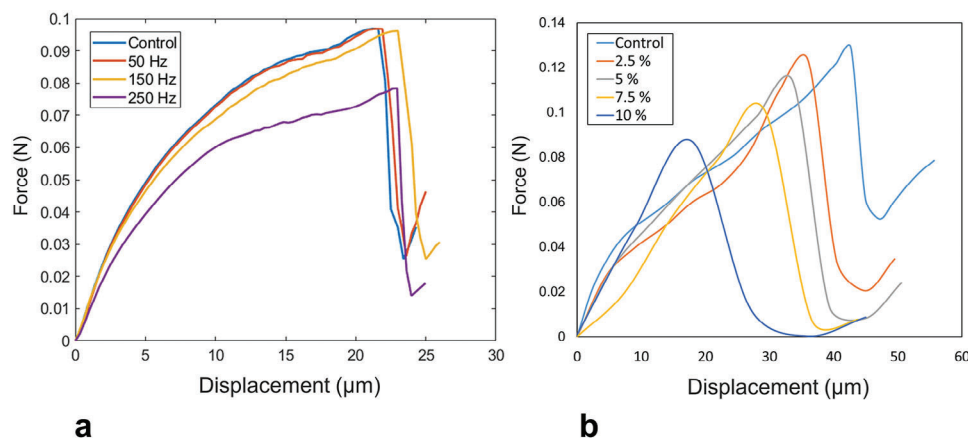


Figure 7. The FEA force-displacement results for a) vibrations between 0–250 Hz and b) strain rates between 0–10%.

LRA frequency vibrations resulted in a 10.98% and 12.88% increase in the FSS concentration compared to the control case (0 Hz). **Figure 9** shows the bar chart with mean and standard deviation error bars ($n = 4$) of FSS concentrations for ERM and LRA-induced vibration experiments.

4. Discussion

4.1. Fabrication of DMNPs

The current study reported on a new multi-stage replication of PVA/PVP DMNPs to reduce the overall replication time. TPP technique was used to fabricate primary master MN arrays. The PDMS negative mold of the primary master MN array was produced for replications of multiple thermoplastic MN arrays through a well-established soft embossing process developed in our group.^[19,24,55] The replicated thermoplastics (Zeonor 1060R) MN arrays had high fidelity, and the PDMS negative molds were intact after >30 replication cycles.^[55] This study used the replicated thermoplastic MN arrays, for the first time, as the secondary masters to make several PDMS molds for the replication of PVA/PVP DMNPs in a short time. This approach reduced the overall fabrication time (combination of the times required for TPP, PDMS micromolding, soft embossing, centrifugation, and curing) from 746 to 98 h per set of ten DMNPs, demonstrating a $\approx 86.9\%$ decrease in the total fabrication time. The PVA/PVP DMNPs exhibited $13.46 \pm 0.31\%$ longitudinal shrinkage compared to the original design parameters and $8.9 \pm 0.32\%$ shrinkage compared to the thermoplastic secondary master MN arrays.^[55] The shrinkage in the size of the final MN replicas from the master MN array signifies the need for design adjustments or slowing the replication process to achieve the required sizing; however, this could significantly increase the production time.

4.2. MN Mechanical Strength

To perform the mechanical tests, DMNPs were fabricated as single PVA/PVP MNs through a process similar to MN patches. The experimental and theoretical studies on com-

pression and bending experiments showed that DMNPs possess sufficient structural integrity for skin insertion and penetration. Due to the skin's irregular structure and the presence of wrinkles, the evaluation of the bending strength of the MNs was equally important to the compression.^[21] The compression results for our PVA/PVP MNs showed a buckling failure of 0.65 ± 0.04 N at the quasi-static condition. However, a bending failure of 0.33 ± 0.02 N was recorded, which is in accordance with Demir et al. bending experiments on (Polyglycolide) PGA MNs with similar geometry and a bending failure of 0.24 ± 0.05 N.^[67] Despite the lower mechanical strength of the PVA/PVP MNs compared to our previously studied thermoplastics MNs,^[55] the SM for PVA/PVP DMNPs was estimated to be ≈ 2.5 , which is well greater than unity ($SM > 1$) that is required for insertion of MNs into the skin without failure.

4.3. MN Insertion Mechanism Using Skin Strain and Vibration

In this study, we used a skin stretching tool^[55] to investigate the mechanism of MN insertion and extraction on the PDMS skin model with different strains (0%, 5%, 10%, 15%, and 20%). The current study used PDMS (1:10 curing agent/base) as the artificial skin model (ASM) with an elastic modulus of 1527 ± 237 Pa,^[68] which was supported by PLA layer acting as skin underlying hard tissues. Makvandi et al. used a similar approach to make a multilayered ASM with highly elastic biomechanical behavior (elastic module $G' \approx 1300 - 1700$ Pa > viscoelastic module G''). Their ASM consists of a silicon layer that imitates the SC and supported by gelatin-based hydrogel capable of mimicking drug diffusion properties and MN penetration.^[69] The results showed 34.4% and 57.8% reductions in the maximum insertion (F_{ins}) and extraction (F_{ext}) forces when the strain value increased from 0% to 20%. Additionally, FEA simulations of MN insertions were conducted on a multilayered hyperelastic skin model with 0%, 2.5%, 5%, 7.5%, and 10% strains. The data showed that increasing the skin strain from 0% to 10% resulted in a 32.31% reduction in F_{ins} . In a similar study, Shu et al. conducted a 3D hyperelastic, anisotropic, pre-stressed MN insertion simulation

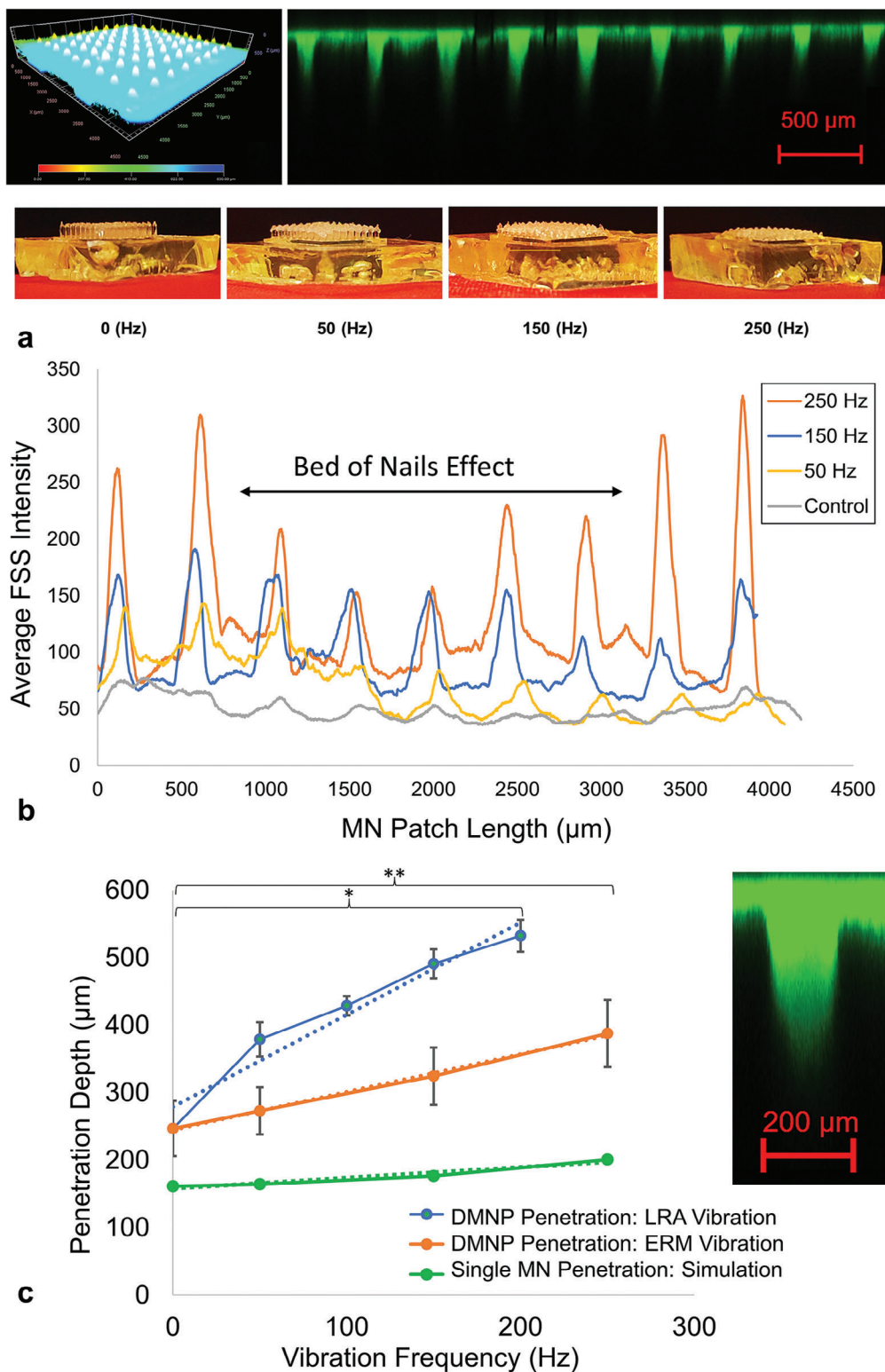


Figure 8. a) Confocal microscope image of DMNPs applied into the porcine cadaver skin at 250 Hz frequency, and the optical images of a typical DMNP dissolution pattern for different ERM vibration frequencies (0 – 250 Hz) 4 min after application into the porcine skin. b) Average FSS diffusion intensity across the entire DMNPs (81 samples) versus MN patch length. The graph shows the bed of nail effects at the central part of the MN patches. c) Penetration depth (μm) of the FSS model drug versus vibration frequency (Hz). The graph compares the data obtained from confocal microscopy for the diffusion depth of the FSS model drug after ≈30 min with the FEA data of MN penetration applied at different vibration frequencies. Data are represented as mean ± SD (* $p < 0.0001$, (**) $p < 0.05$).

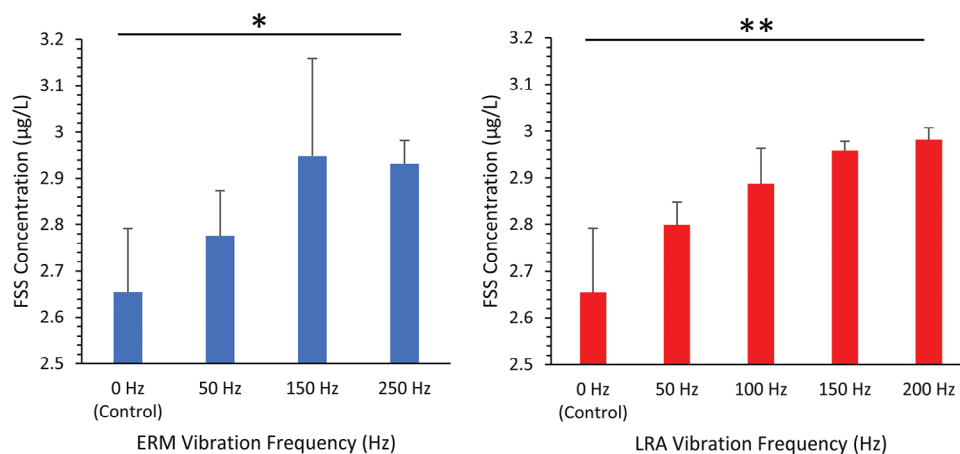


Figure 9. The FSS drug model concentration for ERM and LRA-induced tests at different vibration frequencies. Data are represented as mean + SD, (*) $p < 0.05$, (**) $p < 0.0001$.

model. The results demonstrated that increasing skin pretension from 0% to 10% reduced penetration force by 13%.^[59]

Yang and Zahn previously reported the effect of the vibratory actuator in reducing the F_{ins} from ≈ 0.28 to 0.08 N at an unspecified kHz range.^[46] Here, we applied a low-frequency spectrum ranging from 0 to 250 Hz to measure the insertion and extraction forces of PEN needles on the PDMS artificial skin model. By increasing the frequency to 250 Hz, the F_{ins} reduced by 12.24% from 0.286 N to 0.251 N, while F_{ext} remarkably reduced by 43.01% from 0.093 to 0.057 N. Despite the direct effects of vibratory microdevices on the reduction of insertion and extraction loads, the degree to which force can be reduced depends on different factors, such as the nature of the skin model, relative humidity, skin location, and orientation.^[70]

4.4. Effects of Low-Frequency Vibration on Model Drug Diffusion and Concentration

The diffusion of the FSS model drug was evaluated for a series of LRA and ERM vibrations using maximum FSS diffusion depth and concentration. The results showed increasing the ERM frequency from 50 to 250 Hz improved the diffusion depth by 41.98%, from 273.05 ± 34.98 to 387.68 ± 49.63 μm in 30 min. Application of LRA frequency from 50 to 200 Hz showed a 40.54% increase in FSS diffusion depth from 379.01 ± 25.44 to 532.63 ± 23.69 μm . Due to the nature of excitations, at a constant frequency of 150 Hz, vibration using LRA indicated a 51.35% higher diffusion rate than the ERM. The results were compared to the FEA analysis of MN penetration depth at 3 m s⁻¹ to validate the diffusion depth. For instance, for 50 and 150 Hz, the penetration was 161.12 and 176.52 μm , respectively. When compared to FSS diffusion depth after ≈ 30 min, LRA and ERM diffusions reached 273.05 ± 34.98 and 324.51 ± 42.40 μm in 50 Hz and 379.01 ± 25.44 and 491.14 ± 21.45 μm in 150 Hz, indicating a two-fold average increase in the FSS diffusion depth. In general, the central DMNPs indicated lower diffusion depth due to the “bed of nails” effect, which mainly depends on MN interspacing. The “bed of nails” in a dense MN array is defined as when the skin is locally stretched by the outermost MNs, resulting in the central MNs

exerting the applied force on the stretched skin.^[21] Therefore, a higher applied force is required as the pressure exerted by the individual MN tips is insufficient to penetrate the skin.^[66]

Measurements for the concentration of the FSS model drug showed a direct relationship between the vibrational frequency and dissolution rate. For the case of ERM vibration, increasing vibration from 0 to 250 Hz increased the FSS concentration by 10.98% from 2.64 ± 0.14 to 2.93 ± 0.05 $\mu\text{g L}^{-1}$. The LRA showed a greater improvement of 12.88%, with 2.98 ± 0.03 $\mu\text{g L}^{-1}$ at 200 Hz. The findings also indicated that parts of the DMNP bases which were in contact with porcine skin were dissolved on the skin surface and into the microchannels created after penetration. Similarly, Liu et al. measured TMPH delivery using vertical vibration ranges of 3200, 4800, and 6400 rpm on solid MNs. The results indicated that increasing vibration from 3200 rpm to 6400 rpm resulted in a five-fold increase in TMPH permeation.^[51] Our study tested a relatively higher molecular weight model drug of 376.27 g mol⁻¹, which is more challenging than the study conducted by Liu et al. Seeger et al. also previously reported on the effects of vibration on the dissolution of oral drug formulation. The dissolution degree generally depends on the dissolution method, drug properties, and formulation.^[50] Governing equations for drug diffusion and vibrations in fluid-structure interaction systems are further explained in the Supporting Information.

5. Conclusion

The application of MN technology is becoming a promising method for TDD.^[71,72] This study introduced a procedure for replicating PVA/PVP DMNPs using TPP, soft embossing, and PDMS micromolding techniques. The proposed manufacturing method used MNs made of IP-S and Zeonor 1060R thermoplastic as primary and secondary master structures to create PVA/PVP DMNPs. The overall replication time was reduced by $\approx 86.9\%$ for each set of ten PVA/PVP DMNPs while maintaining high accuracy and fidelity. The replicated PVA/PVP DMNPs successfully penetrated the skin models without buckling or bending failure.

MN insertion and extraction mechanisms were tested for varying vibration frequencies and strains using a rheometer.

Effects of vibration and strains were verified by reducing peak insertion and extraction force during the skin insertions. A simulation paradigm was also introduced for MN penetration into the multilayered skin model with hyperelastic mechanical behavior incorporating skin vibrations and strains. FEA and experimental results confirmed 32.31% and 22.83% reductions in insertion force at 10% skin model strains, respectively. For the case of vibrations, these reductions were 2.1% and 9.8% for insertion force at 150 Hz.

Skin insertion tests were conducted on porcine skin using a novel prototype impact applicator capable of ERM/LRA microvibration. To mimic the skin in vivo condition, a skin stretching mechanism was used to regulate the skin stretch.^[55] The study evaluated the penetration depth, diffusion pattern, and concentrations of a model drug. The results showed LRA and ERM vibrations facilitated the penetration and diffusion of the model drug and enhanced the FSS concentrations. The FSS concentration increased by 11.36% ERM and 12.12% LRA at 150 Hz vibration; an average twofold increase in diffusion depth was recorded for ERM/LRA-induced vibration. In conclusion, applying low-frequency vibration and skin strain considerably improved the insertion and drug diffusion of PVA/PVP DMNPs.

Supporting Information

Supporting Information is available from the Wiley Online Library or from the author.

Acknowledgements

This work was performed in part at the Queensland node of the Australian National Fabrication Facility. A company established under the National Collaborative Research Infrastructure Strategy to provide nano and microfabrication facilities for Australia's researchers. This research was also undertaken partly with the support of resources from the Institute for Advanced Engineering and Space Sciences at the University of Southern Queensland. This research received no specific grants from public, commercial, or not-for-profit funding agencies.

Conflict of Interest

The authors declare no competing interests.

Data Availability Statement

The data that support the findings of this study are available from the corresponding author upon reasonable request.

Keywords

dissolving microneedles, drug delivery, insertion force, low-frequency vibration, skin strain

Received: August 1, 2023
Revised: November 9, 2023
Published online: January 2, 2024

- [1] W. Y. Jeong, M. Kwon, H. E. Choi, K. S. Kim, *Biomater. Res.* **2021**, *25*, 24.
- [2] J. H. Jung, S. G. Jin, *J. Pharm. Investig.* **2021**, *51*, 503.
- [3] M. R. Prausnitz, *Adv. Drug Delivery Rev.* **2004**, *56*, 581.
- [4] R. Jamaledin, P. Makvandi, C. K. Y. Yiu, T. Agarwal, R. Vecchione, W. Sun, T. K. Maiti, F. R. Tay, P. A. Netti, *Adv. Ther.* **2020**, *3*, 2000171.
- [5] G. Ma, C. Wu, C. Wu, **2017**, *J. Controlled Release* **251**, 11.
- [6] J. Yang, X. Liu, Y. Fu, Y. Song, Y. Song, **2019**, *Acta Pharm. Sin. B.* *9*, 469.
- [7] F. Z. Amourizi, A. Z. Malek-Khatibi, R. Zare-Dorabei, *Mater. Chem. Horiz.* **2023**, *2*, 113.
- [8] X. Chen, G. J. P. Fernando, M. L. Crichton, C. Flaim, S. R. Yukiko, E. J. Fairmaid, H. J. Corbett, C. A. Primiero, A. B. Ansaldo, I. H. Frazer, L. E. Brown, M. A. F. Kendall, *J. Control Release* **2011**, *152*, 349.
- [9] M. S. Lee, C. X. Pan, V. E. Nambudiri, *Ther. Adv. Vaccines Immunother* **2021**, *9*, 25151355211039073.
- [10] A. Vander Straeten, M. Sarmadi, J. L. Daristotle, M. Kanelli, L. H. Tostanoski, J. Collins, A. Pardeshi, J. Han, D. Varshney, B. Eshaghi, J. Garcia, T. A. Forster, G. Li, N. Menon, S. L. Pyon, L. Zhang, C. Jacob-Dolan, O. C. Powers, K. Hall, S. K. Alsaiani, M. Wolf, M. W. Tibbitt, R. Farra, D. H. Barouch, R. Langer, A. Jaklenec, *Nat. Biotechnol.* **2023**.
- [11] G.-S. Liu, Y. Kong, Y. Wang, Y. Luo, X. Fan, X. Xie, B.-R. Yang, M. X. Wu, *Biomaterials* **2020**, *232*, 119740.
- [12] K. M. Saifullah, Z. Faraji Rad, *Adv. Mater. Interfaces* **2023**, *10*, 2201763.
- [13] R. Nagarkar, M. Singh, H. X. Nguyen, S. Jonnalagadda, S. Jonnalagadda, *J. Drug Deliv. Sci. Technol.* **2020**, *59*, 101923.
- [14] F. K. Aldawood, A. Andar, S. Desai, *Polymers* **2021**, *13*, 2815.
- [15] R. E. M. Lutton, J. Moore, E. Larrañeta, S. Ligett, A. D. Woolfson, R. F. Donnelly, *Drug Deliv. Transl. Res.* **2015**, *5*, 313.
- [16] H. R. Nejad, A. Sadeqi, G. Kiaee, S. Sonkusale, *Microsyst. Nanoeng* **2018**, *4*, 17073.
- [17] S. Dharadhar, A. Majumdar, S. Dhoble, V. Patravale, V. Patravale, *Drug Dev. Ind. Pharm.* **2019**, *45*, 188.
- [18] A. Malek-Khatibi, Z. Faraji Rad, M. Rad-Malekshahi, H. Akbarijavar, **2023**, *Mater. Lett.* *330*, 133328.
- [19] Z. Faraji Rad, R. E. Nordon, C. J. Anthony, L. Bilston, P. D. Prewett, J.-Y. Arns, C. H. Arns, L. Zhang, G. J. Davies, *Microsyst. Nanoeng.* **2017**, *3*, 17034.
- [20] R. F. Donnelly, T. R. Raj Singh, E. Larrañeta, M. McCrudden, *Microneedles for Drug and Vaccine Delivery and Patient Monitoring*, John Wiley & Sons Ltd, Queen's University Belfast, UK, **2018**, <https://doi.org/10.1002/9781119305101>.
- [21] V. Ebrahiminejad, P. D. Prewett, G. J. Davies, Z. Faraji Rad, *Adv. Mater. Interfaces* **2022**, *9*, 2101856.
- [22] E. Larrañeta, R. E. M. Lutton, A. D. Woolfson, R. F. Donnelly, *Mater. Sci. Eng. R Rep.* **2016**, *104*, 1.
- [23] T. Waghule, G. Singhvi, S. K. Dubey, M. M. Pandey, G. Gupta, M. Singh, K. Dua, K. Dua, *Biomed. Pharmacother.* **2019**, *109*, 1249.
- [24] V. Ebrahiminejad, Z. Faraji Rad, *Adv. Mater. Interfaces* **2022**, *9*, 2201115.
- [25] J. Li, M. Zeng, H. Shan, C. Tong, *Curr. Med. Chem.* **2017**, *24*, 2413.
- [26] Y.-C. Kim, J.-H. Park, M. R. Prausnitz, *Adv. Drug Delivery Rev.* **2012**, *64*, 1547.
- [27] N. Roxhed, T. C. Gasser, P. Griss, G. A. Holzapfel, G. Stemme, G. Stemme, *J. Microelectromech. Syst.* **2008**, *16*, 1429.
- [28] M. R. Prausnitz, *Annu. Rev. Chem. Biomol. Eng.* **2017**, *8*, 177.
- [29] X. Jiang, H. Zhao, W. Li, W. Li, *Front. Bioeng. Biotechnol.* **2022**, *10*, 840395.
- [30] R. F. Donnelly, T. R. R. Singh, M. J. Garland, K. Migalska, R. Majithiya, C. M. McCrudden, P. L. Kole, T. M. T. Mahmood, H. O. Mccarthy, A. D. Woolfson, *Adv. Funct. Mater.* **2012**, *22*, 4879.

- [31] J. G. Turner, L. R. White, P. Estrela, H. S. Leese, *Macromol. Biosci.* **2021**, *21*, e2000307.
- [32] R. Jamaledin, C. K. Y. Yiu, E. N. Zare, L. N. Niu, R. Vecchione, G. Chen, Z. Gu, F. R. Tay, P. Makvandi, *Adv. Mater.* **2020**, *32*, 2002129.
- [33] I. A. Tekko, A. D. Permana, L. Vora, T. Hatahet, H. O. Mccarthy, R. F. Donnelly, *Eur. J. Pharm. Sci.* **2020**, *152*, 105469.
- [34] R. Jamaledin, C. Di Natale, V. Onesto, Z. Taraghdari, E. Zare, P. Makvandi, R. Vecchione, P. Netti, *J. Clin. Med.* **2020**, *542*, 9.
- [35] A. Malek-Khatabi, M. Sadat Razavi, A. Abdollahi, M. Rahimzadeghan, F. Moammeri, M. Sheikhi, M. Tavakoli, M. Rad-Malekshahi, Z. Faraji Rad, *Biomater. Sci.* **2023**, *11*, 5390.
- [36] M. Shikida, S. Kitamura, C. Miyake, K. Bessho, *Microsyst. Technol.* **2014**, *20*, 2239.
- [37] X. Liu, J. Cleary, G. K. German, *Acta Biomater.* **2016**, *43*, 78.
- [38] P. F. Humbert, F., H. Maibach, P. Agache, *Agache's Measuring the Skin*, Springer, Switzerland, **2017**, <https://link.springer.com/referencework/10.1007/978-3-319-32383-1>.
- [39] M. M. Badran, J. Kuntsche, A. Fahr, **2009**, *Eur. J. Pharm. Sci.* *36*, 511.
- [40] M. L. Crichton, A. Ansaldo, X. Chen, T. W. Prow, G. J. P. Fernando, M. A. F. Kendall, *Biomaterials* **2010**, *31*, 4562.
- [41] R. F. Donnelly, M. J. Garland, D. I. J. Morrow, K. Migalska, T. R. R. Singh, R. Majithiya, A. D. Woolfson, *J. Control Release* **2010**, *147*, 333.
- [42] P. Makvandi, M. Kirkby, A. R. J. Hutton, M. Shabani, C. K. Y. Yiu, Z. Baghbantargarhdari, R. Jamaledin, M. Carlotti, B. Mazzolai, V. Mattoli, R. F. Donnelly, *Nanomicro. Lett.* **2021**, *13*, 93.
- [43] S. A. Ranamukhaarachchi, B. Stoeber, B. Stoeber, *Biomed. Microdevices* **2019**, *21*, 100.
- [44] O. Olatunji, D. B. Das, M. J. Garland, L. Belaid, R. F. Donnelly, *J. Pharm. Sci.* **2013**, *102*, 1209.
- [45] B. Ahn, *Int. J. Control, Autom. Syst.* **2019**, *18*, 143.
- [46] M. Yang, J. D. Zahn, *Biomed. Microdevices* **2004**, *6*, 177.
- [47] B. Al-Qallaf, D. B. Das, A. Davidson, A. Davidson, *Asia-Pac. J. Chem. Eng.* **2009**, *4*, 845.
- [48] S. Niamlang, A. Sirivat, *Drug Deliv.* **2009**, *16*, 378.
- [49] M. R. Prausnitz, S. Mitragotri, R. Langer, *Nat. Rev. Drug Discovery* **2004**, *3*, 115.
- [50] N. Seeger, S. Lange, S. Klein, S. Klein, *AAPS PharmSciTech.* **2015**, *16*, 759.
- [51] T.-T. Liu, K. Chen, Q. Wang, Q. Wang, *Drug Deliv. Transl. Res.* **2018**, *8*, 1025.
- [52] S. M. Flaherty, I. J. Russell, A. N. Lukashkin, *Drug Delivery* **2021**, *28*, 1312.
- [53] W. F. Beyer, D. L. Smith, *J. Pharm. Sci.* **1971**, *60*, 496.
- [54] K. Embil, G. Torosian, G. Torosian, *J. Pharm. Sci.* **1979**, *68*, 1336.
- [55] V. Ebrahiminejad, Z. Faraji Rad, P. D. Prewett, G. J. Davies, *Beilstein J. Nanotechnol.* **2022**, *13*, 629.
- [56] Z. Faraji Rad, P. D. Prewett, G. J. Davies, *Add. Manuf.* **2022**, *56*, 102953.
- [57] J.-H. Park, M. G. Allen, M. R. Prausnitz, *J. Control Release* **2005**, *104*, 51.
- [58] O. A. Shergold, N. A. Fleck, D. Radford, *Inter. J. Impact Eng.* **2006**, *32*, 1384.
- [59] W. Shu, H. Heimark, N. Bertollo, D. J. Tobin, E. D. O'cearbhaill, A. N. Annaidh, *Acta Biomater.* **2021**, *135*, 403.
- [60] S. C. Meliga, J. W. Coffey, M. L. Crichton, C. Flaim, M. Veidt, M. A. F. Kendall, *Acta Biomater.* **2017**, *48*, 341.
- [61] N. Jain, V. K. Singh, S. Chauhan, S. Chauhan, *J. Mech. Behavior. Mater.* **2017**, *26*, 213.
- [62] S. A. Ranamukhaarachchi, S. Lehnert, S. L. Ranamukhaarachchi, L. Sprenger, T. Schneider, I. Mansoor, K. Rai, U. O. Häfeli, B. Stoeber, B. Stoeber, *Sci. Rep.* **2016**, *6*, 32074.
- [63] F. H. Silver, G. P. Seehra, J. W. Freeman, D. DeVore, *J. Appl. Polym. Sci.* **2002**, *86*, 1978.
- [64] F. P. Beer, J. T. DeWolf, D. F. Mazurek, *Mechanics of Materials*, McGraw-Hill Education, New York, NY, USA **2015**, <https://www.amazon.com.au/Mechanics-Materials-Ferdinand-P-Beer/dp/0073398233>.
- [65] S. K. Sharma, J. Prakash, P. K. Pujari, *Phys. Chem. Chem. Phys.* **2015**, *17*, 29201.
- [66] M. Gülçür, J.-M. Romano, P. Penchev, T. Gough, E. Brown, S. Dimov, B. Whiteside, B. Whiteside, *CIRP J. Manuf. Sci. Technol.* **2021**, *32*, 311.
- [67] Y. K. Demir, Z. Akan, O. Kerimoglu, *PLOS ONE* **2013**, *8*, e77289.
- [68] F. C. P. Sales, R. M. Ariati, V. T. Noronha, J. E. Ribeiro, *Procedia Struct. Integr.* **2022**, *37*, 383.
- [69] P. Makvandi, M. Shabani, N. Rabiee, Q. K. Anjani, A. Maleki, E. N. Zare, A. H. B. Sabri, D. De Pasquale, M. Koskinopoulou, E. Sharifi, R. Sartorius, M. Seyedhamzeh, S. Bochani, I. Hirata, A. C. Paiva-Santos, L. S. Mattos, R. F. Donnelly, V. Mattoli, *Adv. Mater.* **2023**, *35*, 2370127.
- [70] H. Joodaki, M. B. Panzer, *Proc. Inst. Mech. Eng. H.* **2018**, *232*, 323.
- [71] Y. Ghiyasi, P. D. Prewett, G. J. Davies, Z. Faraji Rad, *Int. J. Pharm.* **2023**, *641*, 123087.
- [72] A. Malek-Khatabi, M. Rad-Malekshahi, M. Shafiei, F. Sharifi, H. Motasadizadeh, V. Ebrahiminejad, M. Rad-Malekshahi, H. Akbarijavar, Z. Faraji Rad, *Biomater. Sci.* **2023**, *11*, 7784.